EJNMMI RESEARCH

ORIGINAL RESEARCH

Open Access

Assessment of early response to neoadjuvant chemotherapy in multi-site high-grade serous ovarian cancer using hyperpolarized-^{13}C MRI

Lucian Beer[1,2*†], Vlad Bura[1,3†], Stephan Ursprung[1,4], Ramona Woitek[1,5], Mary A. McLean[1], Joo Ern Ang[6], Mercedes Jimenez-Linan[7], Andrew B. Gill[1], Joshua Kaggie[1], Matthew Locke[1], Amy Frary[1], Johanna Field-Rayner[1], Ilse Patterson[1], Marika Reinius[8], Martin J. Graves[1], Surrin Deen[1], Gabriel Funingana[6,9,10], Leonardo Rundo[1], Andrew Priest[1], Luigi Aloj[1,11], Roido Manavaki[1,11], Iosif A. Mendichovszky[1,11], Fraser Robb[12], Rolf F. Schulte[13], Dominique-Laurent Couturier[9], Clive S. D'Santos[9], Valar Franklin[9], Kamal Kishore[9], Iris Allajbeu[1], Carolin Sauer[9], Ferdia A. Gallagher[1], Kevin M. Brindle[6,14], James D. Brenton[7,9,10†] and Evis Sala[1,15,16*†]

Abstract

Background To evaluate the capability of hyperpolarized [1-^{13}C] pyruvate MRI to predict pathologic response to neoadjuvant treatment in multi-site abdominopelvic disease of high-grade serous ovarian cancer (HGSOC) patients and to compare ^{13}C MRI and [^{18}F]-FDG PET/CT measurements for detecting early treatment response. We recruited eight patients with HGSOC in this prospective study who underwent ^{13}C MRI and [^{18}F]-FDG PET/CT before and after the first cycle of neoadjuvant chemotherapy treatment (NACT). Imaging parameters were compared with clinical and histophatologic parameters.

Results We demonstrate here that ^{13}C MRI of hyperpolarized [1-^{13}C]pyruvate metabolism in multiple abdominal metastases resulted in rapid labeling of the endogenous tumor lactate pool. The rate of labeling was similar between the different anatomical disease sites and independent of tumor volume. The apparent rate constant describing exchange of ^{13}C label between pyruvate and lactate (k_{PL}) was positively correlated with PET standard uptake values (SUV_{max}) for [^{18}F]-FDG in metastatic tumor deposits in the ovary/pelvis (R = 0.471, P = 0.02). Decreased lactate labeling could be detected after the first cycle of neoadjuvant chemotherapy and was associated with pathological response. There was no overall decrease in lactate labeling in a single patient who lacked a complete histopathologic response. k_{PL} was associated with cancer tissue LDHA concentration (rho = 0.641; P = 0.02).

Conclusion This exploratory study demonstrates the potential of ^{13}C MRI measurements for assessing early response to neoadjuvant chemotherapy in patients with HGSOC.

Keywords Ovarian cancer, Hyperpolarized MRI, Functional imaging, Hybrid imaging, Oncologic imaging

†Lucian Beer and Vlad Bura: share the first authorship

†James D. Brenton and Evis Sala: share the last authorship

*Correspondence:
Lucian Beer
lucian.beer@meduniwien.ac.at
Evis Sala
evis.sala@policlinicogemelli.it
Full list of author information is available at the end of the article

Introduction

High-grade serous ovarian cancer (HGSOC) is characterized by marked intra-tumoral heterogeneity reflecting divergent evolution in both genomic and immunological landscapes [1–5]. These evolutionary changes may result in different patterns of response within a single patient, but cannot be detected using clinical treatment response criteria from computed tomography (CT) and the serum tumor marker CA-125. In addition, tissue sampling of every lesion is not a feasible option for clinical management. For patients receiving neoadjuvant chemotherapy (NACT) prior to delayed primary surgery (DPS), the major clinical challenge is to identify those with non-responding disease. Sequential changes in the levels of CA-125 overestimate response to neoadjuvant therapy [6]. Imaging methods that can accurately predict early and heterogeneous tumor response would enable individualized treatment approaches and provide new tools for studying primary treatment resistance.

Since metabolic changes in response to anti-cancer therapy occur earlier than anatomical changes and metabolic imaging can enable earlier detection of treatment response [7]. HGSOC is characterized by high glycolytic activity and lactate formation [8]. Tumor response after chemotherapy treatment frequently leads to a reduction in lactate labeling from hyperpolarized [1-^{13}C] pyruvate [9, 10], while persistent lactate labeling is usually a marker of treatment failure [11]. In mouse human colorectal and breast adenocarcinoma xenografts, ^{13}C Magnetic Resonance Imaging (MRI) of hyperpolarized [1-^{13}C] pyruvate metabolism was shown to detect earlier treatment-response when compared to [^{18}F]-FDG-PET [9]. Detection of treatment response using ^{13}C MRI of hyperpolarized [1-^{13}C]pyruvate metabolism in humans has only been reported in case series of breast [10, 12] and prostate cancer [13, 14] and has not been compared to detection of treatment response using [^{18}F]-FDG-PET.

The aims of this study were: to (1) evaluate the capability of ^{13}C MRI to predict pathologic response to neoadjuvant treatment in multi-site abdominopelvic disease of HGSOC patients and (2) to compare ^{13}C MRI and [^{18}F]-FDG PET/CT measurements for detecting early treatment response.

Materials and methods

This prospective study conducted at the Cambridge University Hospitals NHS Foundation Trust (Cambridge, UK) was approved by the regional review board (National Research Ethics Service Committee East of England, Cambridge South, Research Ethics Committee number 15/EE/0378; National Institute for Health Research [NIHR] portfolio number 30388). Written informed consent was obtained from all participants.

Study participants

Patients were recruited prospectively at Addenbrooke's Hospital, Cambridge UK between August 2019 and August 2021. Inclusion criteria were 18 years of age or older, histological diagnosis of HGSOC, and planned NACT. Exclusion criteria were the inability to undergo an MRI examination, diabetes or previous treatment for HGSOC.

Clinical data

Patients' medical records were reviewed by a specialist trainee in medical oncology in the 7th year of training (G.F.) under the supervision of a board-certificated medical oncologist (J.B.). The investigators who collected the clinical data were blinded to any imaging information.

Proton MRI

Patients 1 to 5 were imaged on a clinical 3T scanner (MR750; GE Healthcare) and patient 6 to 8 were imaged on a clinical 3T PET/MRI scanner (SIGNA PET/MR, GE Healthcare). The built-in ^{1}H body coil of the MRI system was used to acquire three-dimensional (3D) fast gradient echo scout images, and subsequently, T_1-weighted axial fat-suppressed gradient echo images for ^{13}C MRI planning. Following ^{13}C MRI, diffusion weighted imaging, non-contrast and contrast-enhanced imaging of the abdomen or pelvis were undertaken using a cardiac 32-channel coil on the 3T MRI and a body surface 16-channel receive coil on the 3T PET/MRI. The detailed scan parameters are given in supplementary Table 1.

Carbon-13 MR image acquisition

^{13}C MR images were acquired from regions that contained the largest volume and number of disease sites. These were chosen from the distribution of metastases seen in the standard-of-care CT staging images. Images were acquired on a clinical 3T MR system (MR750) or 3T PET/MRI scanner (SIGNA PET/MR; both from GE Healthcare, Waukesha, WI, USA), using a ^{13}C- clamshell coil for transmission (GE Healthcare) [15] and an eight-channel ^{13}C receive coil (Rapid Biomedical, Rimpar, Germany). An Iterative Decomposition with Shifted Echo times and Least Squares Estimation (IDEAL) spiral chemical shift imaging (CSI) sequence [16] was employed to acquire three

to five axial slices (3 cm thick, 3 mm gap) positioned to cover as many of the masses visible by ^{1}H MRI as possible. Radiofrequency pulses with a nominal flip angle of 15° were applied to acquire a 36 cm field-of-view with a matrix size of 40×40 and a temporal resolution of 4 s for 16 to 20 time points (TR = 0.5 s), starting 12 s after the start of injection of hyperpolarized pyruvate.

Carbon-13 image processing

Processing of ^{13}C images was performed in Matlab (Matlab 2018b, The MathWorks, Natick, MA, U.S.A.) using a combination of GE's MNS Research Pack subroutines and in-house programs. Following gridding and reconstruction of the ^{13}C data, interpolated to an in-plane resolution of 128×128 (nominal pixel size of 2.8×2.8 mm), images from multiple coils were combined using singular value decomposition [17]. Maps of lactate and pyruvate signal intensities were summed over the time course, and the apparent rate constant for exchange of ^{13}C label between pyruvate and lactate (k_{PL}) was estimated using a two-site exchange model and a frequency-domain method [18].

Details regarding the PET and proton image analysis can be found in the supplementary material.

Carbon-13 Image Analysis

Tumor Regions of Interest (ROIs) were drawn manually by R1 on co-registered T_1-weighted proton images and propagated to metabolic maps generated by ^{13}C MRI, using ImageJ V1.52 (NIH, Bethesda, ML, USA). Large confluent ovarian/pelvic masses were segmented as a continuous single volume of interest. Metastatic tumor deposits that were clearly separated were measured individually. Noise was estimated (mean and SD) using the summed images of hyperpolarized ^{13}C-labeled bicarbonate. As described previously, we assumed that the noise distribution in images of the different labeled metabolites would be the same, since all of the images were calculated from the same underlying set of multi-echo time data [19]. The signal-to-noise ratio (SNR) values for pyruvate and lactate ($SNR_{metabolite}$) within each tumor were calculated using the following formula:

$$SNR_{metabolite} = \frac{mean\,SI_{tumor} - mean\,SI_{noise}}{\sqrt{2}SDSI_{noise}}$$

The mean SI_{tumor} is the mean signal intensity of the tumor ROI; the mean and SD of SI_{noise} were calculated from the bicarbonate images. The factor $\sqrt{2}$ accounted for the narrowed Rayleigh distribution of magnitude noise, with an approximate adjustment for the use of multiple receivers [20, 21]. The mean metabolite SNR in the tumor images summed over the time course is referred to as the summed SNR_{PYR} and SNR_{LAC}. The mean and maximum k_{PL} were used to assess tumor metabolism of [1-^{13}C]pyruvate.

Histological analysis

All tissue samples were assessed by a board-certified gynecological pathologist (M. J-L.) with 17 years' experience as described in the supplementary methods.

Mass spectrometry analysis

Protein concentration of LDHA and Actin in HGSOC tissue samples was measured using a Dionex Ultimate 3000 UHPLC system coupled to a Q-Exactive HF mass spectrometer (Thermo Fisher Scientific, San Jose, CA). A detailed description is provided in the supplementary information.

Statistical analysis

Summary statistics: Mean and standard deviation (SD) were used as summary statistics for (approximately) normally distributed continuous variables. Median and range were preferred with skewed data. For categorical variables numbers and percentages of patients with the specific characteristics were reported. Graphs were drawn using GraphPad Prism (version 5.01) and R (version 4.0.2).

Correlation: The level of association between continuous outcomes was assessed by means of Spearman rank correlation coefficient. Estimates and inference (two-sided tests) were obtained using SPSS version 28 (IBM, USA).

Test of equality of the location parameter: The non-parametric Kruskal–Wallis (> 2 groups) and Mann–Whitney-Wilcoxon tests (2 groups) tests were used to assess whether there was a difference in medians between groups under the assumptions of shifted distributions and independence between observations.

Multiplicity correction: Unless stated otherwise, no multiplicity correction was used in order to achieve a power (1 − b) as high as possible given our sample size. In such cases, significance tests should be interpreted as exploratory rather than confirmatory. Bonferroni adjusted *P*-values are referred to as `adj. P' in the text.*Type I error:* α = 0.05 was used for all tests.

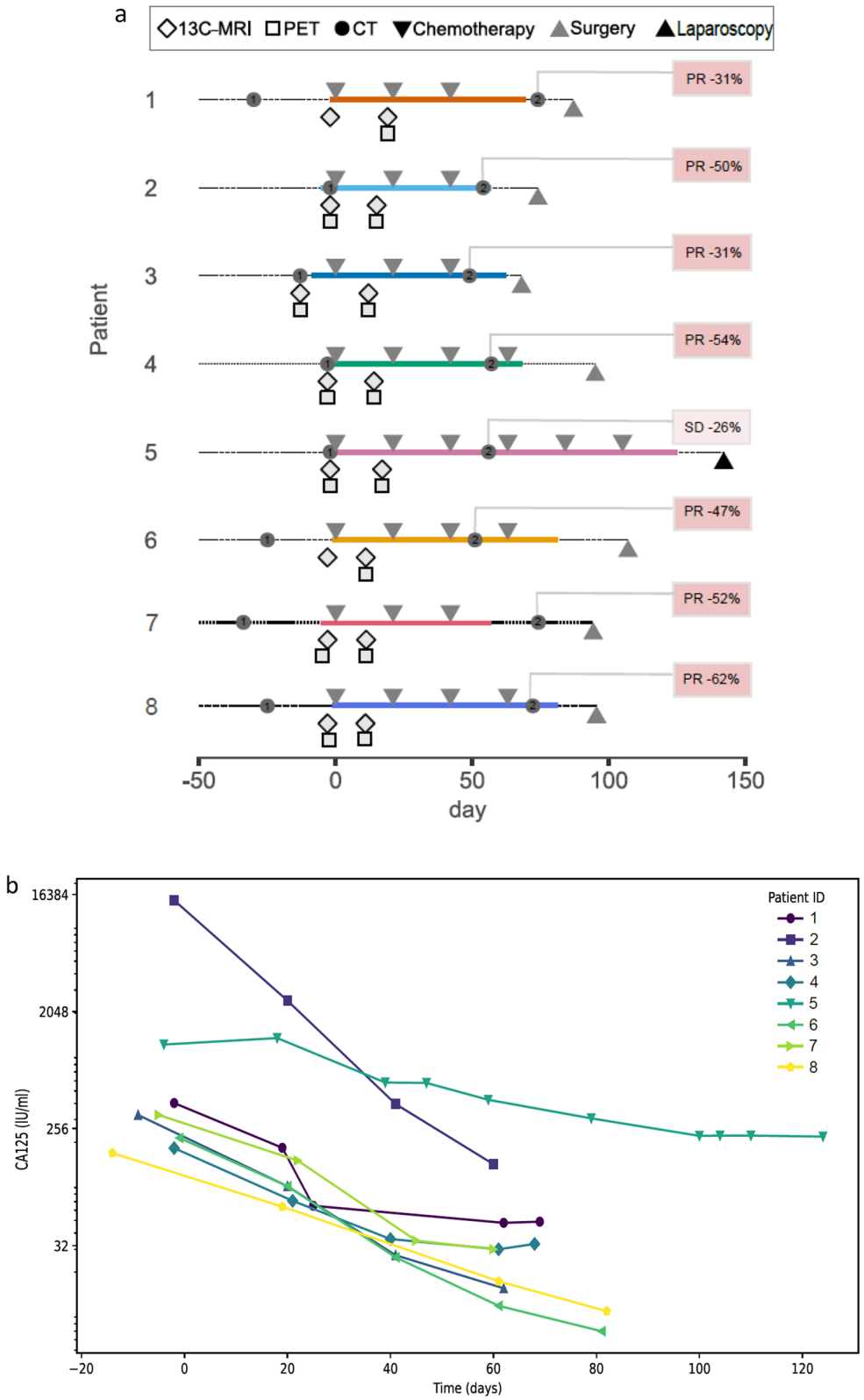

Fig. 1 Overview of the clinical data set.**a** Clinical and study-related interventions for individual patients (y-axis) as a function of time (x-axis). RECIST 1.1 response criteria are shown in shaded boxes (PR partial response, SD stable disease). All patients received carboplatin and paclitaxel chemotherapy, patients 2,3 and 6 additionally received bevacizumab. **b** CA-125 response during neoadjuvant chemotherapy (y-axis) as a function of time from the start of treatment (x-axis)

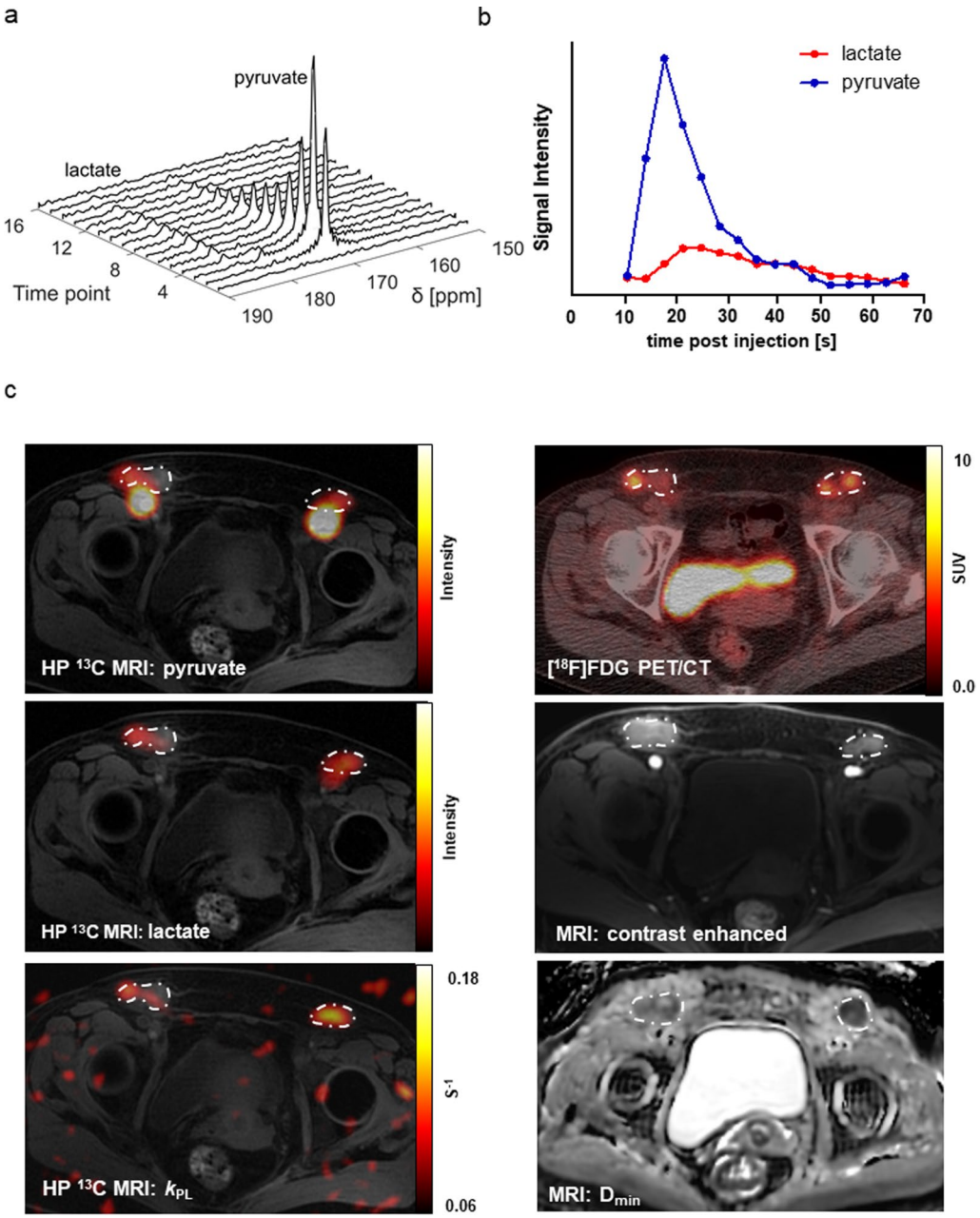

Fig. 2 Mapping metabolic activity in patient 3 using ^{13}C MRI and PET. **a** Stacked plot of 16 dynamic hyperpolarized ^{13}C-spectra from a slice containing the voxels outlined in panel c. **b** Pyruvate and lactate ^{13}C signal intensities in the left inguinal lymph node metastasis shown in panel c at the specified times after hyperpolarized [1-^{13}C]pyruvate injection. **c** 67 year old women with high grade serous ovarian cancer. The corresponding images of hyperpolarized ^{13}C-labeled pyruvate and lactate produced by summing all the images acquired during the time course of lactate labeling and maps of the apparent rate constant describing exchange of ^{13}C label between pyruvate and lactate (k_{PL}), overlaid on an axial T_1-weighted image (left side of the panel). The corresponding [^{18}F]-FDG PET/CT image, contrast-enhanced T_1-weighted image, and ADC (D_{min}) map are shown on the right-hand side. The bilateral metastatic tumor deposits in inguinal lymph nodes are outlined

Results

Patient characteristics, disease distribution, and ^{13}C MRI

Eight patients with histology-proven HGSOC underwent ^{13}C MRI, following injection of hyperpolarized [1-^{13}C] pyruvate, before initiation of NACT and after one cycle (Fig. 1). No adverse effects were observed from [1-^{13}C] pyruvate injection during post-injection monitoring for 1.5 h. All patients received carboplatin and paclitaxel chemotherapy with three patients also receiving bevacizumab (supplementary Tables 2, 3 and Fig. 1).

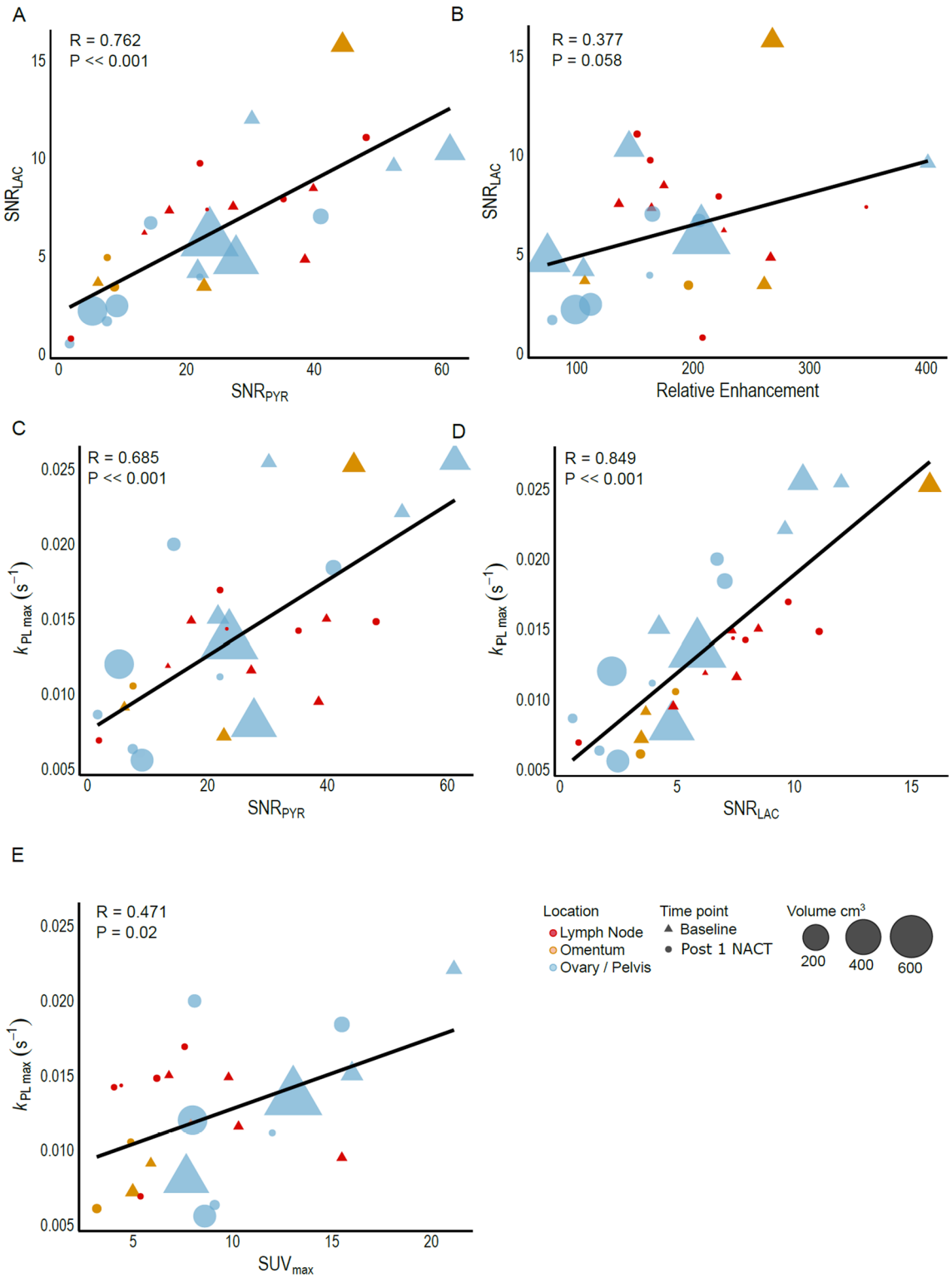

Fig. 3 Correlation of hyperpolarized ^{13}C MR image data with relative gadolinium enhancement and [^{18}F]-FDG uptake. Spearman rank correlations between **a** SNR_{LAC} and SNR_{PYR}, **b** SNR_{LAC} and relative contrast enhancement, **c** $k_{PL\,max}$ and SNR_{PYR}, **d** $k_{PL\,max}$ and SNR_{LAC}, **e** $k_{PL\,max}$ and SUV_{max} obtained from [^{18}F]-FDG PET. Tumors are represented by individual points, with the color and size of the point indicating the tumor location and tumor volume, respectively. P-values (Pearson correlation coefficient) of tests to determine whether the correlations are different from 0 (no correlation) are indicated. The regression lines based on all disease sites are shown in black

Figure 2 shows representative spectra from an acquired slice and time courses of the pyruvate and lactate signal intensities in metastatic tumor deposits in lymph nodes with the corresponding ^{13}C MR, proton MR, and [^{18}F]-FDG PET/CT images. Representative images from all the patients are shown in supplementary Fig. 1.

Delivery of hyperpolarized [1-^{13}C] pyruvate and gadolinium contrast agent correlated with lactate labeling

The rate of lactate labeling depends on delivery of hyperpolarized [1-^{13}C] pyruvate to the tumor via the circulation, uptake into the cell on the monocarboxylate transporters and subsequent exchange of ^{13}C label catalyzed by lactate dehydrogenase. We observed a significant positive correlation between the summed signal-to-noise ratios for lactate (SNR_{LAC}) and pyruvate (SNR_{PYR}) ($R=0.762$; $P \ll 0.001$), and by trend between SNR_{LAC} and the relative gadolinium enhancement ($R=0.377$; $P=0.058$) (Fig. 3A-B). There was also a significant positive correlation between the apparent rate constant describing ^{13}C label exchange between pyruvate and lactate ($k_{PL\ max}$) and the summed SNR_{PYR} ($R=0.685$; $P<<0.001$) (Fig. 3C). Taken together, these data indicate that lactate labeling was dependent on tumor perfusion and pyruvate delivery. This rate constant ($k_{PL\ max}$) was also significantly correlated with SNR_{LAC} ($R=0.849$; $P \ll 0.001$) (Fig. 3D).

We found a positive correlation between SUV_{max} and $k_{PL\ max}$ ($R=0.471$, $P=0.02$) (Fig. 3E). A orrelation is expected between these parameters if increased [^{18}F]-FDG uptake is correlated with increased glycolytic flux and lactate production and LDHA activity is a determinant of the rate of lactate labelling[9].

Pre-treatment pyruvate metabolism is similar between different anatomical disease sites

When analyzing metastatic tumor deposits we found no difference between the medians for the markers $k_{PL\ max}$, and relative contrast enhancement in the ovary/pelvis/peritoneum, omentum and lymph node sites (Fig. 4A-C) (Kruskal–Wallis test: $P>0.05$). A significant difference between the three different sites of disease was noted for the SUV_{max} values (Kruskal–Wallis test: $P=0.04$) and minimum apparent diffusion coefficient (D_{min}), a marker of cell density (Kruskal–Wallis test: $P=0.017$). Further analysis showed that SUV_{max} was higher in the ovary/pelvis/peritoneum compared to the omentum (Mann–Whitney-Wilcoxon test: adj. $P=0.004$). In addition, the levels of D_{min} were significantly lower in omentum compared to the lymph nodes (Fig. 4D) (Mann–Whitney-Wilcoxon test: adj. $P=0.026$). Figure 4E shows pre-treatment ^{13}C MR, proton MR, and [^{18}F]-FDG PET/CT images in patient 2.

Decreased lactate labeling after the first cycle of NACT is associated with pathological response

We then assessed changes in $k_{PL\ max}$ and other imaging parameters after the first cycle of NACT, and correlation with later histopathologic response determined at the time of surgical sampling. Surgical assessment was performed after 3–6 cycles of NACT (Fig. 1a). Figure 5 summarizes the changes in total tumor volume, $k_{PL\ max}$, SNR_{LAC} and SUV_{max} between pre-treatment and after the first cycle of chemotherapy (the data for individual sites are summarized in Fig. 6). The majority of the imaging parameters decreased after one cycle of chemotherapy with the exception of $k_{PL\ max}$, which increased in patient 3 (highlighted in red in Fig. 5C). SUV_{max} showed a non-clinically significant increase (9%) in patient 5. Standard-of-care RECIST measurements, after three cycles of treatment, showed a partial response in all cases except patient 5. Patients 1,2, and 4 to 8 showed partial histopathological response, according to the CRS (omentum) or similar pathological scores at other tumor sites (ovarian metastases in patients 2, 5,6 and 7; lymph node metastases in patient 3 and 8) (Fig. 6A, supplementary Fig. 2). In patient 3, there were areas of no pathological response in metastatic tumor deposits in the omentum and in the left inguinal lymph node and a partial response in the right inguinal and iliac lymph nodes (Fig. 6A, supplementary Fig. 2).

Given the differential response we observed both between patients and between tumor sites, we compared the % changes in $k_{PL\ max}$, SUV_{max}, D_{min} and tumor

(See figure on next page.)

Fig. 4 Inter-site heterogeneity in patient 2 assessed by hyperpolarized ^{13}C MRI, [^{18}F]-FDG PET, relative gadolinium enhancement, and diffusion-weighted imaging. Image in a 59-year old women with high grade serous ovarian cancer. **a** $k_{PL\ max}$, **b** SUV_{max}, **c** relative contrast enhancement, and **d** the diffusion coefficient, *D*, were compared among the three sites of metastasis in pre-treatment images by means of non-parametric Kruskal–Wallis tests (the corresponding adjusted P-values are indicated). **e** Representative images of a patient with ovarian metastases (dashed line) are shown. The lactate and pyruvate images and a map of the calculated k_{PL} are overlaid on an axial T_1-weighted image (left side of the panel). The corresponding [^{18}F]-FDG PET/CT image, contrast-enhanced T_1-weighted image, and ADC (D_{min}) map are shown on the right hand side of the panel

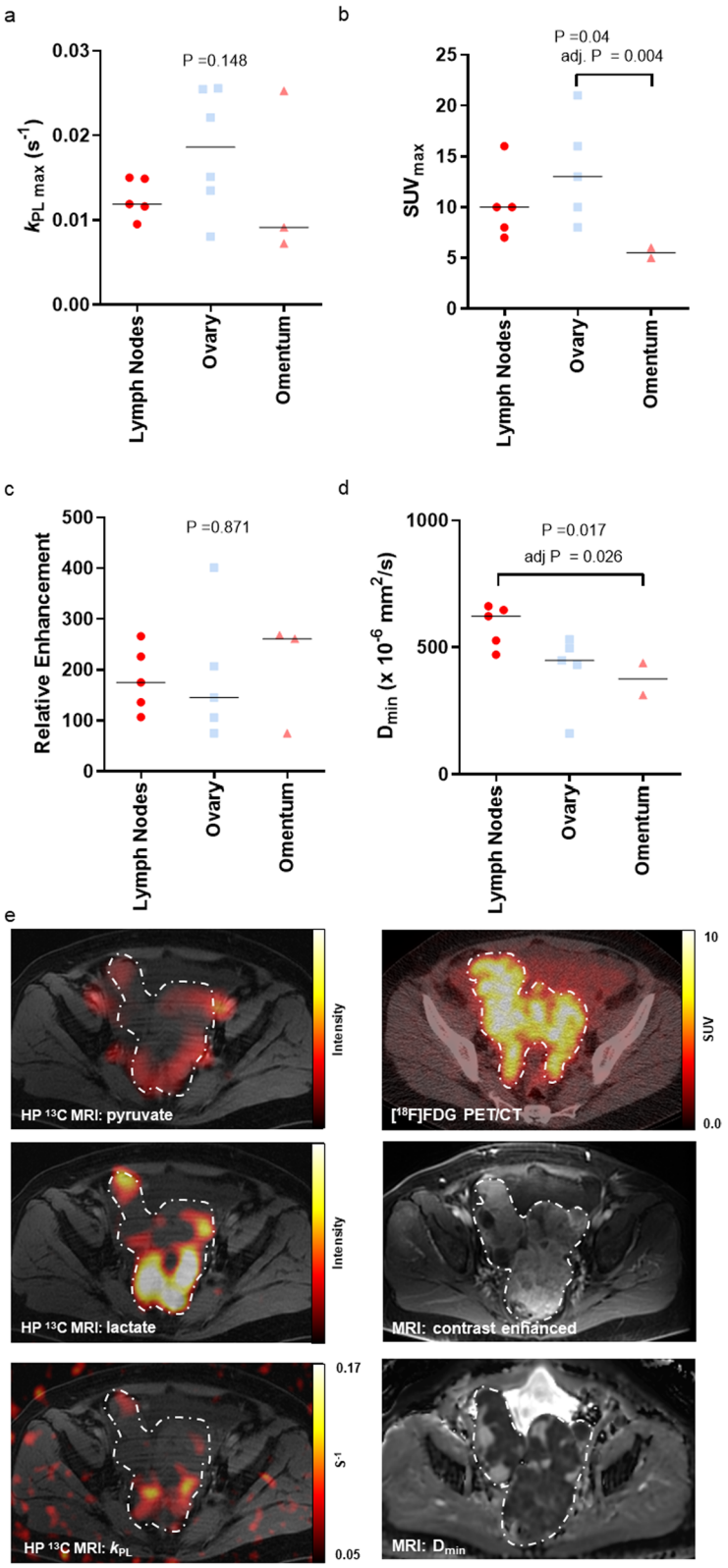

Fig. 4 (See legend on previous page.)

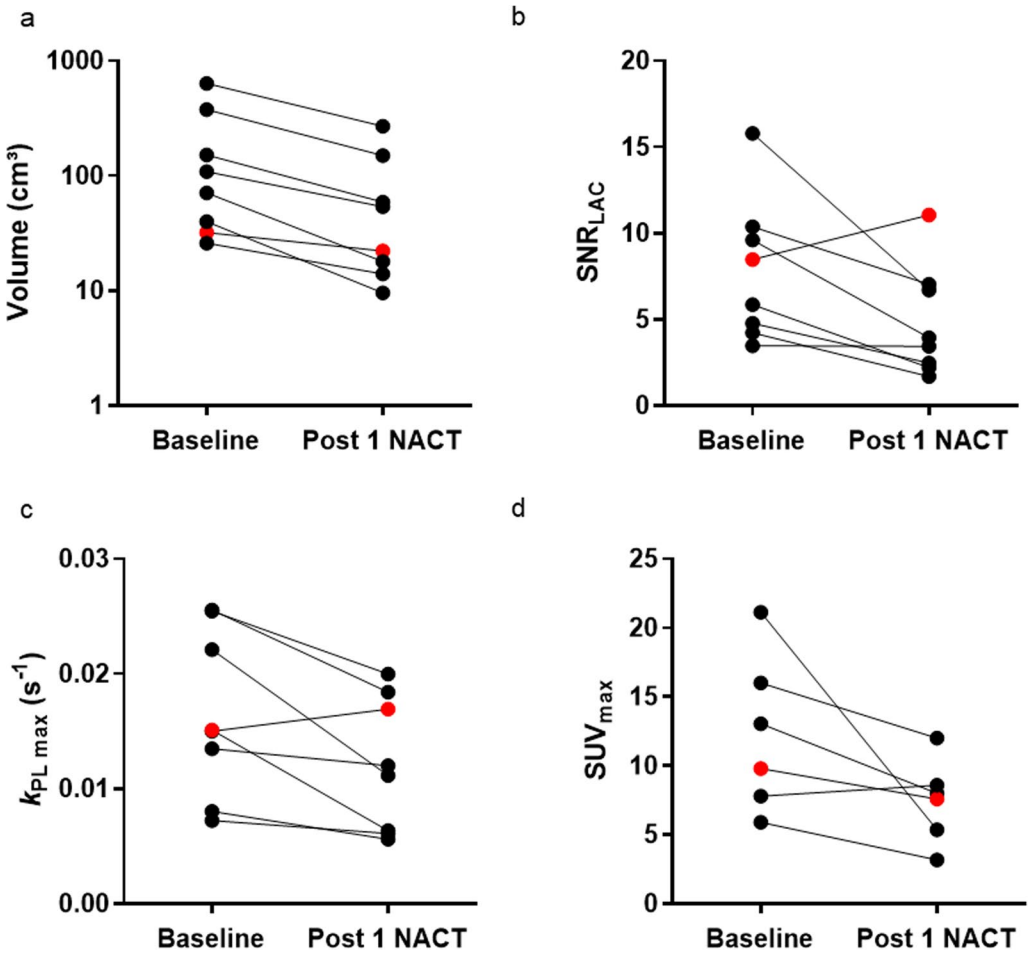

Fig. 5 Assessment of treatment response using hyperpolarized ^{13}C MRI and [^{18}F]-FDG PET. **a** Tumor volume measured on MRI. **b** The SNR_{LAC} and the c the single highest $k_{PL\ max}$ value are given. In d the [^{18}F]-FDG PET parameter SUV_{max}. of the tumor area that is covered by the MR image is given (n = 8 patients for a-c; n = 6 patients for d). Patient 3 (histopathology non responder) is highlighted in red

volume in the four tumor sites in patient 3 with those observed in the other seven patients. Figure 6b shows the corresponding observed values for each marker and group. SUV_{max} and tumor volume decreased and D_{min} increased consistently in all patients following treatment. From visual inspection, the markers $k_{PL\ max}$ and volume seemed to best discriminate responders from non-responders. This assessment is less trivial for SUV_{max} and D_{min}, due to the skewness observed in the responder group. Assuming that within- a patient data are independent and that sites are comparable, we can use statistical inference to test for the equality of the location parameter per group.

Lactate labeling is associated with LDHA tissue protein expression

We then evaluated whether lactate labelling, namely $k_{PL\ max}$ is associated with LDHA tissue concentration. We therefore, compared LDHA concentration of pretherapeutic tissue samples (2 patients, one sample each) and post NACT surgical samples (8 patients, 12 samples) with their corresponding pre-treatment or post 1st cycle NACT MRI. We observed a positive correlation (rho: 0.614; $P = 0.02$; Fig. 7).

Discussion

This study demonstrates that ^{13}C magnetic resonance spectroscopic imaging of hyperpolarized [1-^{13}C]pyruvate metabolism can detect early response to chemotherapy in multi-site advanced stage HGSOC patients. Flux of hyperpolarized ^{13}C label between pyruvate and lactate correlated with tumor perfusion, pyruvate delivery and [^{18}F]-FDG uptake. Of the eight patients examined, one patient did not have a uniform pathological response across all disease sites after three cycles of chemotherapy and uniquely showed increased flux of hyperpolarized ^{13}C label between pyruvate and lactate after the first cycle of treatment. By contrast, the remaining seven patients

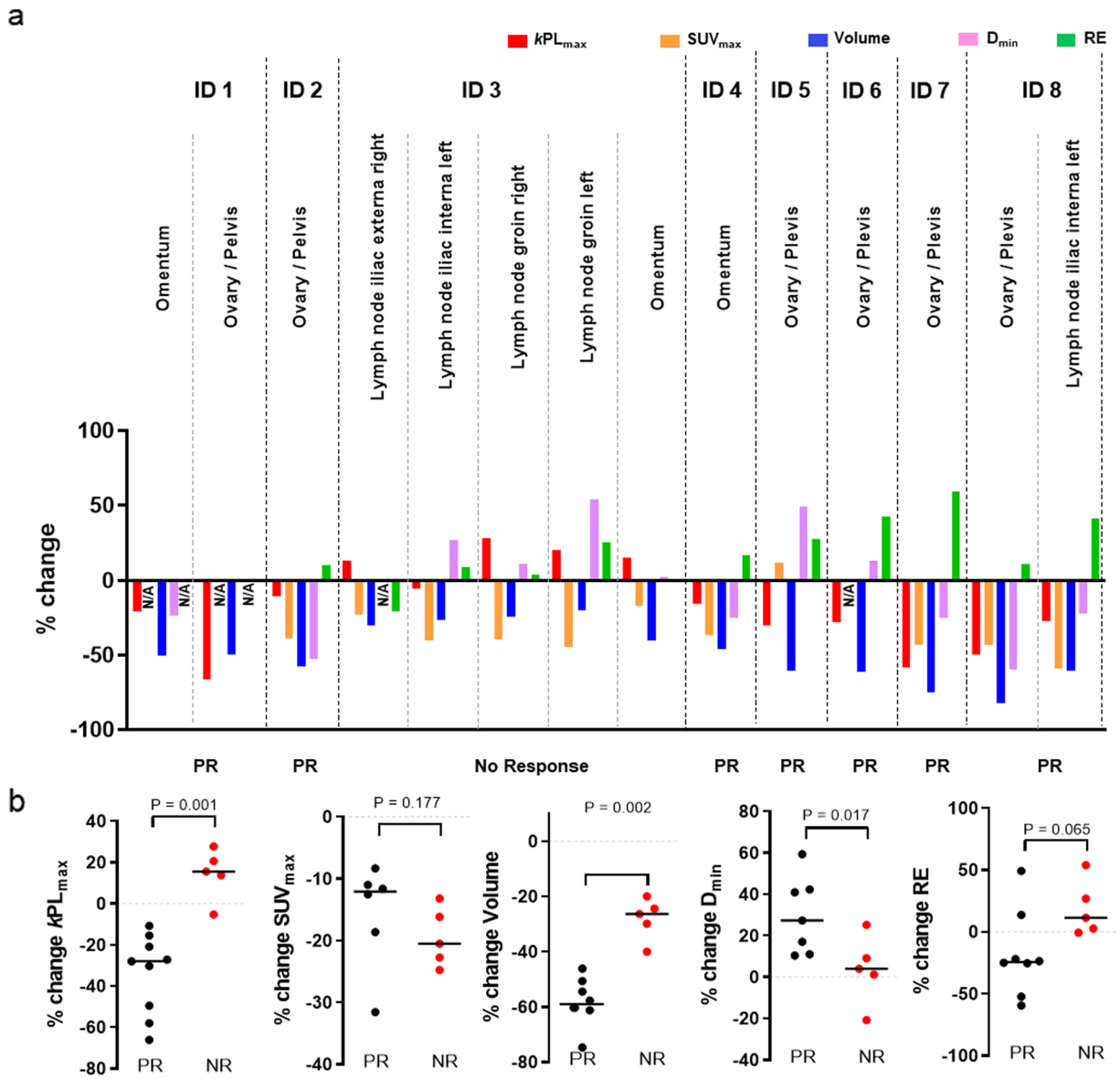

Fig. 6 Correlation of ^{13}C MRI and PET measurements with histopathological markers of treatment response. **a** The relative change in $k_{PL\,max}$, SUV_{max}, tumor volume, D_{min}, relative gadolinium enhancement (RE). PR = partial response. **b** Comparison of marker values for patients showing a partial histopathologic response (patient 1, 2, 4–8, black points) and patient 3, who showed no pathologic response (the four distinct sites of disease for patient 3 are shown as individual red data points). Horizontal black lines correspond to the medians per group. Raw and multiplicity adjusted P-values of Mann–Whitney-Wilcoxon tests are indicated. NR = no-response

all showed uniform pathological response and had a decrease in flux. Tumor volume determined by MRI, and total lesion glycolysis (TLG) and SUV_{max} determined by PET, were unable to discriminate between the non-responding patient and other responding cases.

The potential for clinical use of hyperpolarized [1-^{13}C] pyruvate for detecting treatment response was first demonstrated in pre-clinical models, which showed a reduction in the conversion of pyruvate to lactate following treatment [9, 22–24]. Since then, clinical studies have been performed in patients with breast [10, 12, 19], prostate [14, 25, 26], pancreatic [27] and kidney cancer [28, 29] and glioma [30, 31]. Detection of treatment response has been demonstrated in single case studies in prostate [13, 14] and breast cancer [10], the latter assessing early treatment response. The studies presented here have shown that the technique is capable

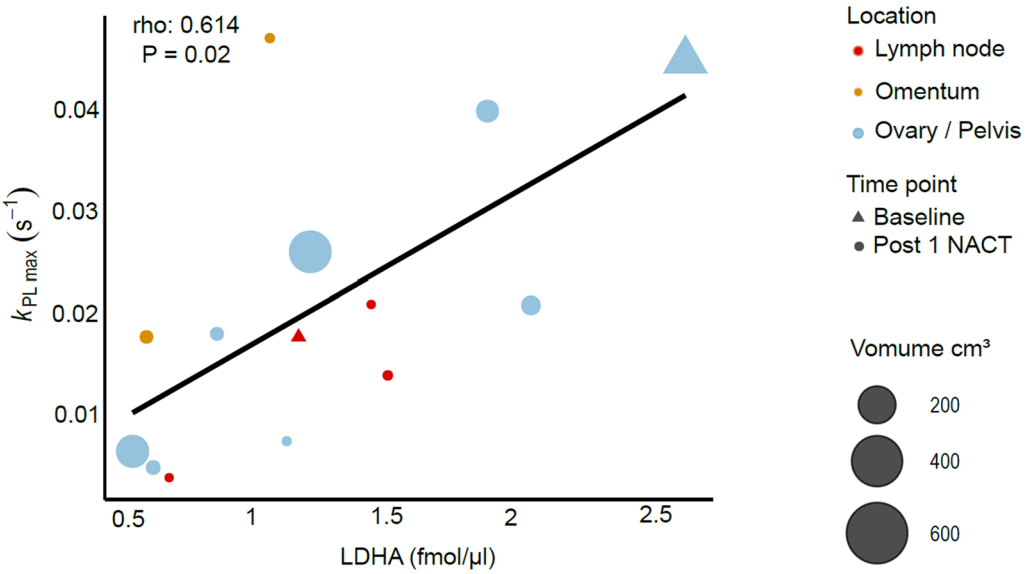

Fig. 7 Correlation between $k_{PL\ max}$ and tissue LDA concentration. Spearman rank correlations between $k_{PL\ max}$ and and tissue LDHA concentration is shown. *P*-values (Pearson correlation coefficient) of tests to determine whether the correlations are different from 0 (no correlation) are indicated. The regression lines based on all disease sites are shown in black

of detecting response, and non-response, in patients with multi-site advanced stage HGSOC following NACT.

Lactate labeling is dependent on pyruvate delivery to the tumor, uptake via the monocarboxylate transporters (MCTs) and ^{13}C label exchange in the reaction catalyzed by lactate dehydrogenase, which in tumors is usually predominantly the A isoform (LDHA) [32] (see supplementary Fig. 3). Importantly we found a positive correlation between LDHA protein concentration and 13C imaging parameters which is in line with previous studies [12, 31, 33]. In addition, we also found a correlation between pyruvate delivery and lactate labeling that was independent of tumor site (metastatic tumor deposits in the ovary/pelvis, omentum, lymph node, or peritoneum) and tumor volume. The lack of an association with volume was also observed in glioma patients but is in contrast to observations from primary breast cancers [19], where labeling was correlated with tumor volume and the expression of HIF1α and MCT1, suggesting that the exchange in this tumor type may be limited by pyruvate uptake.

This study has several limitations. First, this is a small patient population, and for clinical reasons and the COVID-19 pandemic the number of chemotherapy cycles. Prolonged NACT delayed the time interval between ^{13}C MRI and surgery and could have affected the pathological assessment with CRS. In addition, patients were examined using both clinical PET-CT and PET-MRI scanners. However, since FDG values between PET-CT and PET-MRI have been shown to be highly correlated, any impact on this study is expected to be negligible. Another limitation is that we assumed independence between measurements on multiple tumor deposits within a single patient (i.e. different sites of disease can have a different treatment response). Although we believe that this assumption is met in the case of HGSOC the statistical analysis performed has to be interpreted with care. In addition, differences in image slice thicknesses precluded us from performing voxel-based co-registration between ^{13}C MRI, DWI and PET. Although we have made the intriguing observation that increased $k_{PL\ max}$ was associated with absence of pathological response, further mechanistic explanations are needed. It is also important to note that $k_{PL\ max}$ increased in lymph node metastases that subsequently showed partial pathological response suggesting that other processes may be important. These observations need to be further investigated using sensitive molecular analyses of apoptosis and tumor pharmacokinetics. We have developed new methods for targeting biopsies to distinct tumor areas by real-time overlay of CT-derived tumor habitats onto co-registered ultrasound images and are extending our methods to include multi-parametric MRI-derived tumor habitats. This will allow us to target areas of different tumor physiology and metabolism and assess change during treatment so we can better understand the dynamic changes in the tumor microenvironment.

Conclusion

This study has demonstrated the feasibility of imaging hyperpolarized [1-^{13}C] pyruvate metabolism in multi-site metastatic disease in patients with HGSOC and its potential for assessing early treatment response. Larger studies are needed to confirm the potential of ^{13}C MRI to detect early treatment response / treatment failure in patients with HGSOC. If our findings are confirmed in larger numbers of patients, this imaging technique could be used to select patients at high risk of failing standard NACT and to offer them alternative novel treatment options including earlier surgery.

Abbreviations

HGSOC	High grade serous ovarian cancer
kPL	Apparent rate constant
LDHA	Lactate dehydrogenase A
NACT	Neoadjuvant chemotherapy
SUV	Standard uptake value
ADC	Apparent diffusion coefficient
CRS	Chemotherapy response score
SNR	Signal to noise ratio
FDG	Fluorodeoxyglucose

Supplementary Information

The online version contains supplementary material available at https://doi.org/10.1186/s13550-025-01219-5.

Supplementary Material 1.

Acknowledgements

Microsoft Radiomics was provided to the Addenbrooke's Hospital (Cambridge University Hospitals NHS Foundation Trust, Cambridge) by the Microsoft InnerEye project.

Author contributions

Guarantors of integrity of entire study, L.B. V.B, E.S.; study concepts/study design or data acquisition or data analysis/interpretation, all authors; manuscript drafting or manuscript revision for important intellectual content, all authors; approval of final version of submitted manuscript, all authors; agrees to ensure any questions related to the work are appropriately resolved, all authors; literature research, L.B., V.B., R.W., S.U., E.S., J.D.B., K.M.B., M.A.M.; clinical studies, L.B., V.B., R.W., M.A.M., F.A.G. JE.A., J.K., A.F., J.FR., I.P., M.R., C.S., M.J.G., L.R., S.D., IG.F., A.P., L.A., R.M. I.M.J.L; statistical analysis, L.B., R.W., S.U., M.A.M., L.R., A.P., A.G; and manuscript editing, L.B., V.B., S.U., R.W., M.A.M., M.J.L, A.B.G., M.R., L.R., L.A., R.M., I.M., F.R., R.F.S., F.A.G., J.D.B., K.M.B., E.S

Funding

This work was supported by Cancer Research UK (grant numbers: A22905, A15601, A17242), the UK National Cancer Imaging Translational Accelerator (C42780/A27066) and the Mark Foundation for Cancer Research and Cancer Research UK Cambridge Centre (C9685/A25177) and Cambridge Experimental Cancer Medicine Centre. Additional support has been provided by the National Institute of Health Research (NIHR) Cambridge Biomedical Research Centre. The views expressed are those of the authors and not necessarily those of the NHS, the NIHR or the Department of Health and Social Care. Microsoft Radiomics was provided to the Addenbrooke's Hospital (Cambridge University Hospitals NHS Foundation Trust, Cambridge) by the Microsoft InnerEye project. Andrew Priest is supported by the Addenbrooke's Charitable Trust and the National Institute for Health Research [Cambridge Biomedical Research Centre at the Cambridge University Hospitals NHS Foundation Trust].

Availability of data and materials

The datasets generated during and/or analysed during the current study are available from the corresponding author on reasonable request.

Declarations

Ethics approval and consent to participate

This prospective study conducted at the Cambridge University Hospitals NHS Foundation Trust (Cambridge, UK) was approved by the regional review board (National Research Ethics Service Committee East of England, Cambridge South, Research Ethics Committee number 15/EE/0378; National Institute for Health Research [NIHR] portfolio number 30388). Written informed consent was obtained from all participants.

Consent for publication

All authors of the manuscript have read and agreed to its content and are accountable for all aspects of the accuracy and integrity of the manuscript in accordance with ICMJE criteria. That the article is original, has not already been published in a journal, and is not currently under consideration by another journal. That you agree to the terms of the SpringerOpen Copyright and License Agreement, which we strongly recommend you read and, where applicable, Open Data policy. For authors who are prevented from being the copyright holder (for instance where Crown Copyright applies or researchers are US government employees), SpringerOpen can accommodate non-standard copyright lines. If this applies to you, please contact us and provide details of your situation.

Competing interests

Rolf Schulte and Fraser Robb are employees from GE Healthcare. The remaining authors declare no potential conflicts of interest.

Author details

[1]Department of Radiology and Cancer Research UK Cambridge Center, Cambridge CB2 0QQ, UK. [2]Department of Biomedical Imaging and Image-Guided Therapy, Medical University Vienna, 1090 Vienna, Austria. [3]Department of Radiology and Medical Imaging, County Clinical Emergency Hospital, Cluj-Napoca, Romania. [4]Department of Diagnostic and Interventional Radiology, University Hospital Tuebingen, Tuebingen, Germany. [5]Research Center for Medical Image Analysis and Artificial Intelligence (MIAAI), Danube Private University, 3500 Krems, Austria. [6]Addenbrooke's Hospital, Cambridge University Hospitals NHS Foundation Trust, Cambridge CB2 0QQ, UK. [7]Department of Pathology, Addenbrooke's Hospital, Cambridge CB2 0QQ, UK. [8]Cancer Research UK Cambridge Institute, University of Cambridge, Cambridge CB2 0RE, UK. [9]Department of Oncology, Department of Oncology, Hutchison/MRC Research Centre, University of Cambridge, Cambridge CB2 0XZ, UK. [10]Cancer Research UK Cambridge Center, Cambridge CB2 OQQ, UK. [11]Department of Nuclear Medicine, Cambridge University Hospitals NHS Foundation Trust, Cambridge Biomedical Campus, Hills Road, Cambridge CB2 0QQ, UK. [12]GE Healthcare, Inc., Aurora, OH 44202, USA. [13]GE Healthcare, Munich, Germany. [14]Department of Biochemistry, University of Cambridge, Hopkins Building, Tennis Court Road, Cambridge CB2 1QW, UK. [15]Dipartimento Diagnostica per Immagini, Fondazione Policlinico Universitario Agostino Gemelli IRCCS, Radioterapia Oncologica ed Ematologia, Rome, Italy. [16]Dipartimento di Scienze Radiologiche ed Ematologiche, Universita Cattolica del Sacro Cuore, Rome, Italy.

Received: 12 September 2024 Accepted: 7 March 2025
Published online: 17 April 2025

References

1. Jiménez-Sánchez A, Memon D, Pourpe S, Veeraraghavan H, Li Y, Vargas HA, Gill MB, Park KJ, Zivanovic O, Konner J, Ricca J. Heterogeneous tumor-immune microenvironments among differentially growing metastases in an ovarian cancer patient. Cell. 2017;170(5):927–38.
2. Macintyre G, Goranova TE, De Silva D, Ennis D, Piskorz AM, Eldridge M, Sie D, Lewsley LA, Hanif A, Wilson C, Dowson S. Copy number signatures and mutational processes in ovarian carcinoma. Nat Genet. 2018;50(9):1262–70.
3. Zhang AW, McPherson A, Milne K, Kroeger DR, Hamilton PT, Miranda A, Funnell T, Little N, de Souza CP, Laan S, LeDoux S. Interfaces of malignant and immunologic clonal dynamics in ovarian cancer. Cell. 2018;173(7):1755–69.

4. Schwarz RF, Ng CK, Cooke SL, Newman S, Temple J, Piskorz AM, Gale D, Sayal K, Murtaza M, Baldwin PJ, Rosenfeld N. Spatial and temporal heterogeneity in high-grade serous ovarian cancer: a phylogenetic analysis. PLoS Med. 2015;12(2):e1001789.
5. Jiménez-Sánchez A, Cybulska P, Mager KL, Koplev S, Cast O, Couturier DL, Memon D, Selenica P, Nikolovski I, Mazaheri Y, Bykov Y. Unraveling tumor–immune heterogeneity in advanced ovarian cancer uncovers immunogenic effect of chemotherapy. Nat Genet. 2020;52(6):582–93.
6. Clamp AR, McNeish IA, Dean A, Gallardo-Rincon D, Kim JW, O'Donnell DM, Hook J, Blagden S, Brenton JD, Naik R, Perren TJ. Response to neoadjuvant chemotherapy in ICON8: a GCIG phase III randomised trial evaluating weekly dose-dense chemotherapy integration in first-line epithelial ovarian/fallopian tube/primary peritoneal carcinoma (EOC) treatment. Ann Oncol. 2018;29:viii336.
7. Brindle K. New approaches for imaging tumour responses to treatment. Nat Rev Cancer. 2008;8:94–107.
8. Fabian C, Koetz L, Favaro E, Indraccolo S, Mueller-Klieser W, Sattler UG. Protein profiles in human ovarian cancer cell lines correspond to their metabolic activity and to metabolic profiles of respective tumor xenografts. FEBS J. 2012;279(5):882–91.
9. Hesketh RL, Wang J, Wright AJ, Lewis DY, Denton AE, Grenfell R, Miller JL, Bielik R, Gehrung M, Fala M, Ros S. Magnetic resonance imaging is more sensitive than PET for detecting treatment-induced cell death–dependent changes in glycolysis. Cancer Res. 2019;79(14):3557–69.
10. Woitek R, McLean MA, Gill AB, Grist JT, Provenzano E, Patterson AJ, Ursprung S, Torheim T, Zaccagna F, Locke M, Laurent MC. Hyperpolarized 13C MRI of tumor metabolism demonstrates early metabolic response to neoadjuvant chemotherapy in breast cancer. Radiol Imaging Cancer. 2020;2(4):e200017.
11. Mignion L, Acciardo S, Gourgue F, Joudiou N, Caignet X, Goebbels RM, Corbet C, Feron O, Bouzin C, Cani PD, Machiels JP. Metabolic imaging using hyperpolarized pyruvate-lactate exchange assesses response or resistance to the EGFR Inhibitor cetuximab in patient-derived HNSCC xenografts. Clin Cancer Res. 2020;26(8):1932–43.
12. Woitek R, McLean MA, Ursprung S, Rueda OM, Manzano Garcia R, Locke MJ, Beer L, Baxter G, Rundo L, Provenzano E, Kaggie J. Hyperpolarized carbon-13 MRI for early response assessment of neoadjuvant chemotherapy in breast cancer patients. Cancer Res. 2021;81(23):6004–17.
13. Aggarwal R, Vigneron DB, Kurhanewicz J. Hyperpolarized 1-[^{13}C]-pyruvate magnetic resonance imaging detects an early metabolic response to androgen ablation therapy in prostate cancer. Eur Urol. 2017;72:1028.
14. Chen HY, Aggarwal R, Bok RA, Ohliger MA, Zhu Z, Lee P, Gordon JW, van Criekinge M, Carvajal L, Slater JB, Larson PE. Hyperpolarized ^{13}C-pyruvate MRI detects real-time metabolic flux in prostate cancer metastases to bone and liver: a clinical feasibility study. Prostate Cancer Prostatic Dis. 2020;23(2):269–76.
15. Tropp J, Lupo JM, Chen A, Calderon P, McCune D, Grafendorfer T, Ozturk-Isik E, Larson PE, Hu S, Yen YF, Robb F. Multi-channel metabolic imaging, with SENSE reconstruction, of hyperpolarized [1-^{13}C] pyruvate in a live rat at 3.0 tesla on a clinical MR scanner. J Magn reson. 2011;208(1):171–7.
16. Wiesinger F, Weidl E, Menzel MI, Janich MA, Khegai O, Glaser SJ, Haase A, Schwaiger M, Schulte RF. IDEAL spiral CSI for dynamic metabolic MR imaging of hyperpolarized [1-13C] pyruvate. Magn Reson Med. 2012;68(1):8–16.
17. Rodgers CT, Robson MD. Receive array magnetic resonance spectroscopy: whitened singular value decomposition (WSVD) gives optimal Bayesian solution. Magn Reson Med. 2010;63:881–91.
18. Khegai O, Schulte RF, Janich MA, Menzel MI, Farrell E, Otto AM, Ardenkjaer-Larsen JH, Glaser SJ, Haase A, Schwaiger M, Wiesinger F. Apparent rate constant mapping using hyperpolarized [1–^{13}C] pyruvate. NMR Biomed. 2014;27(10):1256–65.
19. Gallagher FA, Woitek R, McLean MA, Gill AB, Manzano Garcia R, Provenzano E, Riemer F, Kaggie J, Chhabra A, Ursprung S, Grist JT. Imaging breast cancer using hyperpolarized carbon-13 MRI. Proc Natnl Acad Sci. 2020;117(4):2092–8.
20. Gilbert G. Measurement of signal-to-noise ratios in sum-of-squares MR images. J Magn Reson Imaging: Off J Int Soc Magn Reson Med. 2007;26:1678–1678.
21. Constantinides CD, Atalar E, McVeigh ER. Signal-to-noise measurements in magnitude images from NMR phased arrays. Magn Reson Med. 1997;38:852–7.
22. Day SE, Kettunen MI, Gallagher FA, Hu DE, Lerche M, Wolber J, Golman K, Ardenkjaer-Larsen JH, Brindle KM. Detecting tumor response to treatment using hyperpolarized ^{13}C magnetic resonance imaging and spectroscopy. Nat Med. 2007;13(11):1382–7.
23. Oshima N, Ishida R, Kishimoto S, Beebe K, Brender JR, Yamamoto K, Urban D, Rai G, Johnson MS, Benavides G, Squadrito GL. Dynamic imaging of LDH inhibition in tumors reveals rapid in vivo metabolic rewiring and vulnerability to combination therapy. Cell Rep. 2020;30(6):1798–810.
24. Day SE, Kettunen MI, Cherukuri MK, Mitchell JB, Lizak MJ, Morris HD, Matsumoto S, Koretsky AP, Brindle KM. Detecting response of rat C6 glioma tumors to radiotherapy using hyperpolarized [1-^{13}C] pyruvate and ^{13}C magnetic resonance spectroscopic imaging. Magn Reson Med. 2011;65(2):557–63.
25. Granlund KL, Tee SS, Vargas HA, Lyashchenko SK, Reznik E, Fine S, Laudone V, Eastham JA, Touijer KA, Reuter VE, Gonen M. Hyperpolarized MRI of human prostate cancer reveals increased lactate with tumor grade driven by monocarboxylate transporter 1. Cell Metab. 2020;31(1):105–14.
26. Nelson SJ, Kurhanewicz J, Vigneron DB, Larson PE, Harzstark AL, Ferrone M, Van Criekinge M, Chang JW, Bok R, Park I, Reed G. Metabolic imaging of patients with prostate cancer using hyperpolarized [1-^{13}C] pyruvate. Sci Trans Med. 2013;5(198):198ra108.
27. Stødkilde-Jørgensen H, Laustsen C, Hansen ES, Schulte R, Ardenkjaer-Larsen JH, Comment A, Frøkiær J, Ringgaard S, Bertelsen LB, Ladekarl M, Weber B. Pilot study experiences with hyperpolarized [1-^{13}C] pyruvate MRI in pancreatic cancer patients. J Magn Reson Imaging. 2020;51(3):961–3.
28. Tran M, Latifoltojar A, Neves JB, Papoutsaki MV, Gong F, Comment A, Costa AS, Glaser M, Tran-Dang MA, El Sheikh S, Piga W. First-in-human in vivo non-invasive assessment of intra-tumoral metabolic heterogeneity in renal cell carcinoma. BJR Case Rep. 2019;5(3):20190003.
29. Ursprung S, Woitek R, McLean MA, Priest AN, Crispin-Ortuzar M, Brodie CR, Gill AB, Gehrung M, Beer L, Riddick AC, Field-Rayner J. Hyperpolarized ^{13}C-pyruvate metabolism as a surrogate for tumor grade and poor outcome in renal cell carcinoma—a proof of principle study. Cancers. 2022;14(2):335.
30. Park I, Larson PE, Gordon JW, Carvajal L, Chen HY, Bok R, Van Criekinge M, Ferrone M, Slater JB, Xu D, Kurhanewicz J. Development of methods and feasibility of using hyperpolarized carbon-13 imaging data for evaluating brain metabolism in patient studies. Magn Reson Med. 2018;80(3):864–73.
31. Zaccagna F, McLean MA, Grist JT, Kaggie J, Mair R, Riemer F, Woitek R, Gill AB, Deen S, Daniels CJ, Ursprung S. Imaging glioblastoma metabolism by using hyperpolarized [1-^{13}C] pyruvate demonstrates heterogeneity in lactate labeling: a proof of principle study. Radiol Imaging Cancer. 2022;4(4):e210076.
32. Witney TH, Kettunen MI, Brindle KM. Kinetic modeling of hyperpolarized ^{13}C label exchange between pyruvate and lactate in tumor cells. J Biol Chem. 2011;286:24572–80.
33. Sushentsev N, McLean MA, Warren AY, Benjamin AJ, Brodie C, Frary A, Gill AB, Jones J, Kaggie JD, Lamb BW, Locke MJ. Hyperpolarised ^{13}C-MRI identifies the emergence of a glycolytic cell population within intermediate-risk human prostate cancer. Nat Commun. 2022;13(1):466.

Publisher's Note